

## Evaluation of Acoustic Propagation Paths into the Human Head

**Prof. Dr. William D. O'Brien, Jr. and Ms. Yuhui Liu**

Bioacoustics Research Laboratory

Department of Electrical and Computer Engineering

University of Illinois

405 N. Mathews

Urbana, IL 61801

United States of America

Email: [wdo@uiuc.edu](mailto:wdo@uiuc.edu) / [yuhuiliu@uiuc.edu](mailto:yuhuiliu@uiuc.edu)

### **SUMMARY**

*The overall goal has been to develop an acoustic wave propagation model using well-understood and documented computational techniques that track and quantify an air-borne incident acoustic wave propagated around, into and in the human head. This model serves as a computational tool to elucidate the acoustic wave propagation around, into and in the human head. Specifically, the model determines two features: (1) alternate acoustic propagation paths to the cochlear shell that exist besides the normal air-borne acoustic propagation path (eardrum-ossical path) through the auditory canal and (2) sound pressure amplitude in the cochlear shell (relative to the air-borne sound pressure amplitude) via the alternate propagation paths. A 3D finite-element solid mesh was constructed using a digital image database of an adult male head. Coupled acoustic-mechanical finite-element analysis (FEA) was used to model the wave propagation through the fluid-solid-fluid media. The pressure field in fluid media and the displacement field in solid structures were computed at each time step. Instantaneous acoustic pressure waveforms were recorded at various positions inside and outside of the head model, and propagation trajectories (ray paths) were constructed and evaluated from wavefront normals as a function of frequency and incidence angle. The acoustic loss across the skull was estimated to be approximately 33 dB, consistent with theoretical estimates. The computational ray-path results and the theoretical solutions calculated using Snell's law gave a 0.7° difference for low-angle incidence; 10° difference was obtained for larger angle incidence.*

### **1.0 INTRODUCTION**

The overall objective of the proposed program is the development of an acoustic wave propagation model using well-understood and documented computational techniques that track an air-borne incident acoustic wave propagated around, into and in the human head. This model will serve as a computational tool to elucidate the acoustic wave propagation around, into and in the human head to evaluate alternate acoustic propagation paths that exist besides the normal air-borne acoustic propagation path (eardrum-ossical path) through the auditory canal to the cochlea, a cavity in the temporal bone. Specifically, the computational model will evaluate bone conduction that is produced from a sound field in air, and track the bone-conduction acoustic propagation paths into the cochlear shell.

The validation testing of the computational model will involve human subject testing. The interplay between human subject (experimental) testing and theoretical modeling has always benefited the advancement of science. The theoretical model provides a known fundamental basis, and the experiment provides the

O'Brien, Jr., W.D.; Liu, Y. (2005) Evaluation of Acoustic Propagation Paths into the Human Head. In *New Directions for Improving Audio Effectiveness* (pp. 15-1 – 15-24). Meeting Proceedings RTO-MP-HFM-123, Paper 15. Neuilly-sur-Seine, France: RTO. Available from: <http://www.rto.nato.int/abstracts.aps>.

<b>Report Documentation Page</b>			<i>Form Approved OMB No. 0704-0188</i>	
<p>Public reporting burden for the collection of information is estimated to average 1 hour per response, including the time for reviewing instructions, searching existing data sources, gathering and maintaining the data needed, and completing and reviewing the collection of information. Send comments regarding this burden estimate or any other aspect of this collection of information, including suggestions for reducing this burden, to Washington Headquarters Services, Directorate for Information Operations and Reports, 1215 Jefferson Davis Highway, Suite 1204, Arlington VA 22202-4302. Respondents should be aware that notwithstanding any other provision of law, no person shall be subject to a penalty for failing to comply with a collection of information if it does not display a currently valid OMB control number.</p>				
1. REPORT DATE <b>01 APR 2005</b>	2. REPORT TYPE <b>N/A</b>	3. DATES COVERED <b>-</b>		
4. TITLE AND SUBTITLE  <b>Evaluation of Acoustic Propagation Paths into the Human Head</b>			5a. CONTRACT NUMBER	
			5b. GRANT NUMBER	
			5c. PROGRAM ELEMENT NUMBER	
6. AUTHOR(S)			5d. PROJECT NUMBER	
			5e. TASK NUMBER	
			5f. WORK UNIT NUMBER	
7. PERFORMING ORGANIZATION NAME(S) AND ADDRESS(ES) <b>Bioacoustics Research Laboratory Department of Electrical and Computer Engineering University of Illinois 405 N. Mathews Urbana, IL 61801 United States of America</b>			8. PERFORMING ORGANIZATION REPORT NUMBER	
9. SPONSORING/MONITORING AGENCY NAME(S) AND ADDRESS(ES)			10. SPONSOR/MONITOR'S ACRONYM(S)	
			11. SPONSOR/MONITOR'S REPORT NUMBER(S)	
12. DISTRIBUTION/AVAILABILITY STATEMENT <b>Approved for public release, distribution unlimited</b>				
13. SUPPLEMENTARY NOTES <b>See also ADM001856, New Directions for Improving Audio Effectiveness (Nouvelles orientations pour l'amélioration des techniques audio)., The original document contains color images.</b>				
14. ABSTRACT				
15. SUBJECT TERMS				
16. SECURITY CLASSIFICATION OF:			17. LIMITATION OF ABSTRACT <b>UU</b>	18. NUMBER OF PAGES <b>24</b>
a. REPORT <b>unclassified</b>	b. ABSTRACT <b>unclassified</b>	c. THIS PAGE <b>unclassified</b>	19a. NAME OF RESPONSIBLE PERSON	

evidence to evaluate the model. When the experimental and modeling results essentially agree, then a basis is provided to understand at a fundamental level why the experiment performs in the way it does. Further, and most important, with the model validated against experimental observations, the model then becomes a valuable tool to test other hypotheses without the need to conduct expensive and time consuming experiments.

## **2.0 MOTIVATION AND OBJECTIVE**

Noise-induced hearing loss (NIHL) has been an important issue for many years. Human beings that are exposed to excessively high levels of noise can result in temporary hearing loss or permanent hearing damage, *e.g.*, crews that must work near military aircraft are subject to severe noise environments, with Sound Pressure Levels (SPL) reaching 145 to 150 dB. Even a single impulse exposure per day to such intense sounds exceeds permissible noise exposure rules [OSHA 1910.95]. Different hearing protection devices (HPDs) have been designed to prevent NIHL, such as earplugs, earmuffs and helmets. However, there is a limit to how much attenuation can be achieved by protecting the ear canals with muffs and/or plugs, because they do not attenuate sounds that are conducted to the inner ear by the hard and soft tissues of the head and body.

Bone-conduction pathways have been hypothesized for nearly the past three-quarters of a century [Guild 1936; Barany 1938; Wever 1954] and are still largely unknown [Sohmer 2000; Sohmer 2004]. However, some bone-conduction pathways have been proposed, but most of the work to deduce these pathways has been *via* direct contact methods with some type of vibrating device [Wever 1954; Freeman 2000; Sohmer 2000; Stefan 2004]. Human beings sense air-borne sound transmitted by bone conduction when the sound pressure of the external field is about 60 dB above the threshold required for hearing *via* the eardrum-ossical path [Békésy 1948; Zwislocki 1957]. This suggests that noise above 60 dB SPL cannot be fully attenuated by covering or blocking the auditory canal.

When individuals are exposed to severe noise environments, such as those generated by aircraft engines and military weapons that approach and even exceed 150 dB SPL, even if hearing protection equipment is worn, they may be subject to hearing damage. Furthermore, NIHL at low frequencies (*e.g.*, 250 Hz and less) are even more challenging. Thus, for very high noise environments and within certain frequency ranges, conventional HPDs do not provide sufficient protection.

Thus, the goal of the proposed program is to deduce bone-conduction pathways into the cochlear shell. From such knowledge, the design of advanced HPDs can then be based on well-founded scientific fundamentals; it should be noted, however, that the program's goal does not include the development of advanced HPDs.

The normal hearing process termed "air transmission" or "eardrum-ossical path" refers to air-borne sound entering the auditory canal and transduced by the organ of Corti. However, other propagation path processes are considered for purposes of this study. The process, termed "bone conduction," refers to sound entering at any location other than the auditory canal and transduced by the organ of Corti, that is, other than the eardrum-ossical path. The term bone conduction does not necessary imply that the propagation path is entirely bone. The distinction between these two processes (eardrum-ossical path and bone conduction) is necessary because the acoustic propagation paths are evaluated *via* finite-element analysis (FEA) procedures, and the eardrum-ossical path is not included in the evaluation.

For purposes of this study, sound levels will be computationally evaluated to and in the region referred to as the cochlear shell, a cavity that is located in the highly porous temporal bone that contains the organ of Corti. The cochlear response is a vectorial integration of the air-conduction pathway, different bone-conduction pathways, and any other potential alternative pathways. It is possible that each of these pathways is more

effective at different frequencies. Improving the current hearing protection devices thus focuses the need to better understand the sound propagation around, into and inside of the human head, to evaluate different propagation pathways and the paths that are taken to the cochlea.

### 3.0 FUNDAMENTALS FOR VALIDATION STUDIES

#### 3.1 Wave Equation

The necessary assumptions used in ANSYS acoustic analysis include:

- The fluid is compressible, but only relatively small pressure changes with respect to the mean pressure are allowed.
- The fluid is inviscid (no viscous dissipation).
- There is no mean flow of the fluid.
- The mean density and mean equilibrium pressure are uniform throughout the fluid.

The acoustic wave equation is given by [Pierce 1989]

$$\frac{\partial^2 P}{\partial t^2} - c^2 \nabla^2 P = 0, \quad (1)$$

where  $P$  is the acoustic pressure,  $c$  is the sound speed in the fluid medium,  $t$  is time and  $\nabla$  is the Laplacian operator.

The finite-element statement of the wave equation is given by

$$[M_e^P] \{ \ddot{P}_e \} + [K_e^P] \{ \ddot{P}_e \} + \rho_0 [R_e]^T \{ \ddot{u}_e \} = \{ 0 \}, \quad (2)$$

where

$$[M_e^P] = \frac{1}{c^2} \int_{vol} \{ N \} \{ N \}^T d(vol) \text{ is the fluid mass matrix} \quad (2a)$$

$$[K_e^P] = \int_{vol} [B]^T [B] d(vol) \text{ is the fluid stiffness matrix} \quad (2b)$$

$$\rho_0 [R_e] = \rho_0 \int_s \{ N \} \{ n \}^T \{ N' \}^T d(S) \text{ is the fluid-structure coupling mass matrix} \quad (2c)$$

$\{ N \}$  is the element shape function for pressure

$\{ N' \}$  is the element shape function for displacements

$\{ P_e \}$  is the nodal pressure vector

$\{ u_e \} = \{ u_{xe} \}, \{ u_{ye} \}, \{ u_{ze} \}$  is the nodal displacement component vectors

$\{ n \}$  is the unit normal at the fluid boundary

$vol$  is the volume of domain

$S$  is the surface where the derivative of pressure normal to the surface is applied

Well-characterized analytical solutions [Morse 1968] are compared with the finite-element simulation results to validate the analysis.

### 3.2 Scattering by Rigid Cylinder (2D Rigid Cylinder Case)

The acoustic scattering from a rigid cylinder of radius  $a$  due to a plane wave propagating in a direction perpendicular to the cylinder's axis is given by

$$\begin{aligned}
 p_{\text{inc}} &= P_0 e^{ik(r \cos \phi - ct)} = P_0 [J_0(kr) + 2 \sum_{m=1}^{\infty} i^m \cos(m\phi) J_m(kr)] e^{-i\omega t} \\
 p_{\text{sca}} &= \sum_{m=0}^{\infty} A_m \cos(m\phi) [J_m(kr) + iN_m(kr)] e^{-i\omega t} \\
 A_m &= -\varepsilon_m P_0 i^{m+1} e^{-i\gamma_m} \sin \gamma_m \\
 \tan \gamma_0 &= -\frac{J_1(ka)}{N_1(ka)}, \quad \tan \gamma_m = \frac{J_{m-1}(ka) - J_{m+1}(ka)}{N_{m+1}(ka) - N_{m-1}(ka)},
 \end{aligned} \tag{3}$$

where

$p_{\text{inc}}$  is the incident plane wave

$p_{\text{sca}}$  is the scattered wave

$a$  is the cylinder radius

$r$  is the radial distance from the center of the cylinder

$\phi$  is the axial angle for cylindrical coordinates

$c$  is the speed of sound in the medium surrounding the cylinder

$k$  is the  $\omega/c = 2\pi/\lambda$ , wavenumber

$\gamma_m$  is the phase shift

$\varepsilon_m = 1$  when  $m = 0$ ;  $\varepsilon_m = 2$  when  $m > 0$

The total acoustic pressure at the surface of the cylinder at an angle  $\phi$  relative to the  $x$  axis is given by

$$p_a = p_{\text{inc}} + p_{\text{sca}} = \frac{4P_0}{\pi ka} e^{-i\omega t} \sum_{m=0}^{\infty} \frac{\cos(m\phi)}{E_m} e^{i[-\gamma_m + (\pi m/2)]}, \tag{4}$$

where  $E_m$ , the radiation amplitude for a cylinder, is

$$E_0 \approx \sqrt{\frac{8}{2\pi ka}}, \quad E_{m>0} \approx \sqrt{\frac{2}{\pi ka}}, \tag{4a}$$

when  $ka \gg m + 1/2$ , and

$$E_0 \approx \frac{4}{\pi ka}, \quad E_{m>0} \approx \frac{m!}{2\pi} \left(\frac{2}{ka}\right)^{m+1}, \tag{4b}$$

when  $ka \ll m + 1/2$ .

### 3.3 Scattering by Rigid Sphere (3D Rigid Sphere Case)

The acoustic scattering from a rigid sphere of radius  $a$  due to a plane wave propagating to the right along the polar axis is given by

$$p_{\text{inc}} = P_0 e^{ik(r \cos \theta - ct)} = P_0 \sum_{m=0}^{\infty} (2m+1) i^m P_m(\cos \theta) j_m(kr) e^{-i\omega t}$$

$$p_{\text{sca}} = -P_0 \sum_{m=0}^{\infty} (2m+1) i^m e^{-i\delta_m} \sin \delta_m P_m(\cos \theta) [j_m(kr) + i n_m(kr)] e^{-i\omega t} \quad (5)$$

where  $p_{\text{sca}}$  is the wave scattered from the sphere whose center is the polar origin. The total acoustic pressure at a point on the sphere an angle  $\theta$  relative to the polar axis (note that the point  $\theta = 0^\circ$  is the location farthest away from the source of the sound) is given by

$$p_a = (p_{\text{inc}} + p_{\text{sca}})_{r=a} = P_0 (ka)^{-2} \sum_{m=0}^{\infty} \frac{(2m+1)}{B_m} P_m(\cos \theta) e^{-i(\delta_m - \frac{1}{2}\pi m - \omega t)} \quad (6)$$

$$\approx (1 + \frac{3}{2} i k a \cos \theta) P_0 e^{-i\omega t}, \quad ka \ll 1$$

### 3.4 Scattering by Nonrigid Sphere (3D Elastic Sphere Case)

The scattering from a sphere that is not perfectly rigid is more complicated. The total acoustic pressure at a point on the sphere an angle  $\theta$  relative to the polar axis (note that the point  $\theta = 0^\circ$  is the point farthest away from the source of the sound) is given by

$$p_a = P_0 \sum_{m=0}^{\infty} (2m+1) i^m P_m(\cos \theta) [j_m(kr) - \frac{1}{2} (1 + R_m) h_m(kr)], \quad (7)$$

where

$$R_m, \text{ the reflection coefficient, is } 1 + R_m = 2 \frac{j'_m(ka) + i \beta_m j_m(ka)}{h'_m(ka) + i \beta_m h_m(ka)} \quad (7a)$$

$$\beta_m, \text{ the effective admittance, is } \beta_m = i \frac{\rho c}{\rho_e c_e} \left[ \frac{j'_m(k_e a)}{j_m(k_e a)} \right] \quad (7b)$$

$$k_e = \omega/c_e$$

$\rho, c$  are the density and speed of the medium surrounding the sphere

$\rho_e, c_e$  are density and speed of the sphere material

## 4.0 VALIDATION STUDIES

The ANSYS (ANSYS, Inc., Canonsburg, PA) finite-element analysis (FEA) general processing code for both harmonic and transient solutions has been validated using well-understood two-dimensional (2D) and three-dimensional (3D) models. Harmonic (continuous-wave) validation studies were conducted for (1) 2D rigid cylinder, (2) 3D rigid sphere and (3) 3D elastic sphere. Transient (one-cycle sine wave) validation studies were conducted for (1) homogeneous air, (2) 2D elastic cylinder shell, and (3) 3D elastic (water) sphere. For all of the validation studies, either a harmonic or transient acoustic plane wave was initiated in air. The air-borne acoustic wave was incident on the geometric model that was either rigid, elastic or water. Water is an ideal fluid for this study because it has acoustic propagation properties similar to those of brain and other soft tissues. In all cases, the computational solutions of acoustic pressure distribution agreed well with the analytic solutions of acoustic pressure distribution.

To be familiar with different types of acoustic analysis in ANSYS and ensure building our FEA model in a proper way, several case studies were carried out on different geometric models. For these validation studies, the simulation results are compared with the theoretical solutions to evaluate the model. Herewith are the symbols used:

$f$  = center frequency of the incident wave (kHz)

$c$  = sound speed in the medium (m/s)

$\lambda$  = wavelength in the medium (m)

$\rho$  = material density ( $\text{kg}/\text{m}^3$ )

$a$  = cylinder radius / shell outer radius /sphere radius (3D) (m)

$d$  = shell thickness (m)

$r$  = radial distance from the center of the cylinder

BOUND = FEA absorbing boundary radius (m)

$\varphi_{\text{inc}}$  = incident angle, the angle between incident wave and  $+x$  axis (degree)

$X_{\text{inc}}$  = incident wave position (m)

$P_{\text{inc}}$  = incident wave pressure amplitude (Pa)

$T$  = period of the incident wave

DPW = number of mesh divisions per wavelength

ITS = integration time step size

### 4.1 2D Rigid Cylinder (Harmonic Analysis Case)

Figure 1 shows the FEA model used in ANSYS for the 2D rigid cylinder case (§3.2). The air-borne incident harmonic plane wave propagates in the  $+x$ -axis direction. When the propagating wave meets the rigid cylinder target, acoustic pressure is distributed around the cylinder surface.

Parameters:

$f = 3 \text{ kHz}$   
 $c_{\text{air}} = 340 \text{ m/s}$   
 $\lambda_{\text{air}} = 340 / 3000 = 0.113 \text{ m}$   
 $\rho_{\text{air}} = 1.2 \text{ kg/m}^3$   
 $a = 0.4 \lambda_{\text{air}} = 0.0452 \text{ m}$   
 $\text{BOUND} = 1.4 \lambda_{\text{air}} = 0.158 \text{ m}$   
 $\phi_{\text{inc}} = 0^\circ$   
 $X_{\text{inc}} = -0.625 \lambda_{\text{air}} = 0.0706 \text{ m}$   
 $P_{\text{inc}} = 1 \text{ Pa}$   
 $\text{DPW} = 20$

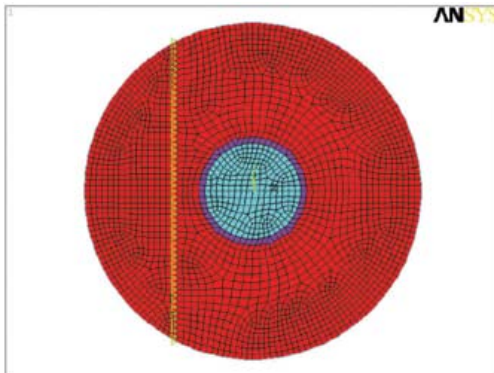


**Fig 1: The 2D rigid cylinder FEA model generated by ANSYS. Red: air; Light blue: rigid cylinder; Dark blue: connecting elements; Yellow: location of plane wave initiation.**

Figure 2 shows the ANSYS simulation results (circles) of the pressure distribution on the cylinder surface compared with the analytical solutions (line), and along the radial component. Good agreement is obtained.

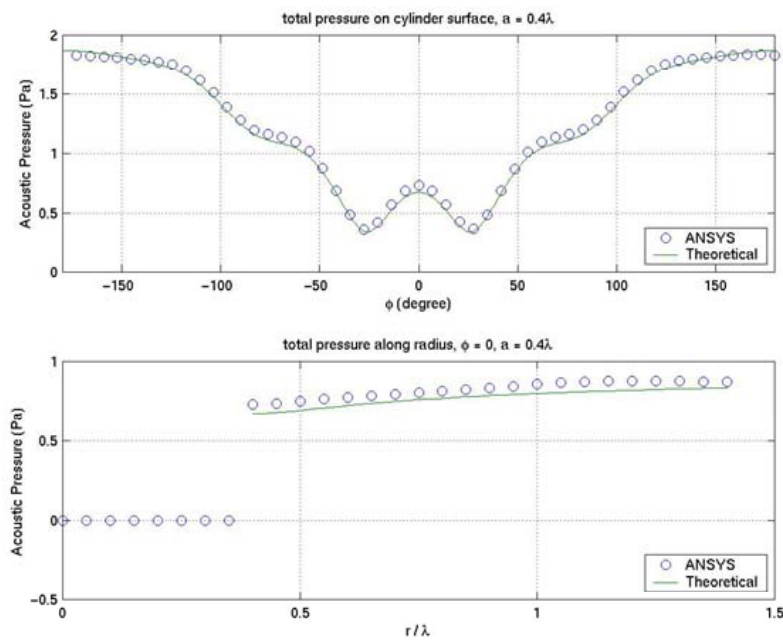


Fig 2: 2D rigid cylinder simulation results (circles) vs. analytical solutions (lines). Top plot: total pressure on cylinder surface (note that the point  $\phi = 0^\circ$  is the point farthest away from the source of the sound). Bottom plot: total pressure along radius, observation angle  $\phi = 0^\circ$  (note that  $r$  = radial distance from the center of the cylinder).

#### 4.2 3D Rigid Sphere (Harmonic Analysis Case)

Figure 3 shows the FEM model used in ANSYS for the 3D rigid sphere case (§3.3). The air-borne incident harmonic plane wave propagates in the  $+x$ -axis direction. This case is of considerable practical importance because many scattering objects are more or less spherical. When the propagating wave meets the rigid spherical target, acoustic pressure is distributed around the spherical surface.

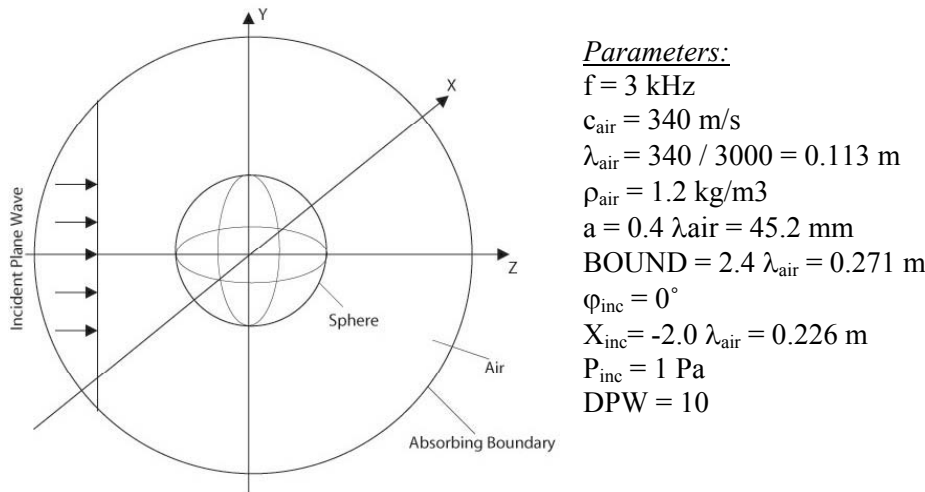


Fig 3: The 3D rigid and nonrigid sphere FEA model.

Figure 4 shows the ANSYS simulation results (circles) of the pressure distribution on the spherical surface compared with the analytical solutions (line), and along the radial component. Good agreement is obtained.

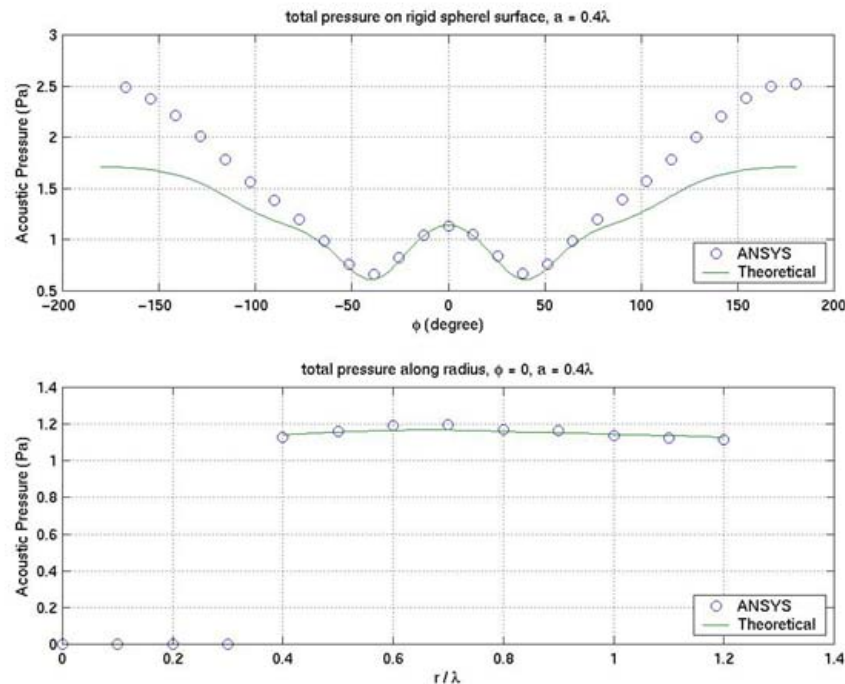


Fig 4: 3D rigid sphere simulation results (circles) vs. analytical solutions (lines). Top plot: total pressure on the surface of the center sphere cross section (note that the point  $\phi = 0^\circ$  is the point farthest away from the source of the sound). Bottom plot: total pressure along  $+z$  axis, observation angle  $\phi = 0^\circ$  (note that  $r =$  radial distance from the center of the sphere).

#### 4.3 3D Elastic Sphere (Harmonic Analysis Case)

For the perfectly rigid cases (§4.1 and §4.2) the propagated wave does not enter the object. However, for real objects, the propagated acoustic wave will enter the object. Figure 3 shows the FEA model used in ANSYS for the 3D nonrigid sphere case (§3.4). Here the nonrigid sphere's density and speed are assumed to be twice those of air (parameters same as in Fig 3 except for  $c_{\text{sphere}} = 680 \text{ m/s}$  and  $\rho_{\text{sphere}} = 2.4 \text{ kg/m}^3$ ). The air-borne incident harmonic plane wave propagates in the  $+x$ -axis direction. This case is of considerable practical importance because many scattering objects are more or less spherical. When the propagating wave meets the nonrigid spherical target, acoustic pressure is distributed around the spherical surface, and also enters into the sphere.

Figure 5 shows the ANSYS simulation results (circles) of the pressure distribution on the elastic spherical surface compared with the analytical solutions (line), and along the radial component. Fair agreement is obtained.

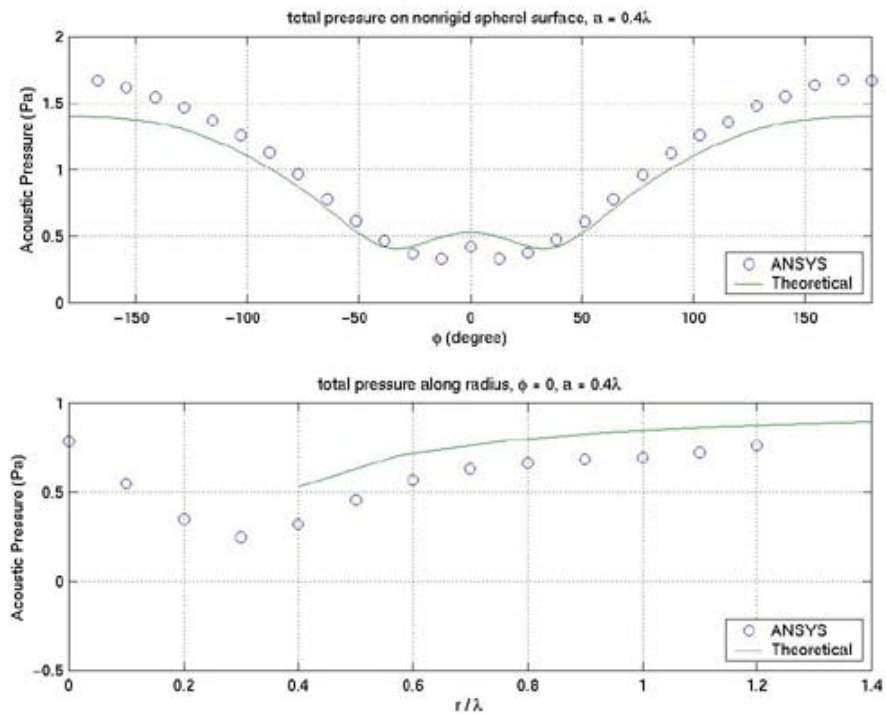


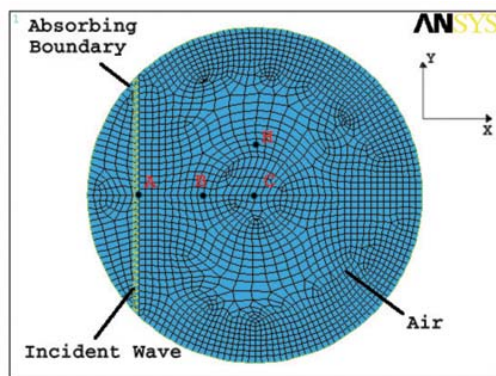
Fig 5: 3D elastic sphere simulation results (circles) vs. analytical solutions (lines). Top plot: total pressure on the surface of the center sphere cross section (note that the point  $\phi = 0^\circ$  is the point farthest away from the source of the sound). Bottom plot: total pressure along  $+z$  axis, observation angle point  $\phi = 0^\circ$  (note that  $r$  = radial distance from the center of the sphere).

#### 4.4 2D Analysis in Homogenous Media (Transient Analysis Case)

Transient analysis is a more realistic approach than harmonic analysis for modeling the incident acoustic pressure waveforms onto and in the human head. However, transient analysis is more involved because it requires added computer resources and more of *our* resources, in terms of the “engineering” time involved.

To save a significant amount of these resources, preliminary studies were conducted to understand further the physics of the problem for validation purposes, that is, analyzing a simpler model provides better insight into the problem at minimal cost.

The 2D transient analysis (air is treated as the object) is evaluated to determine whether the computation domain space introduces artifacts. Here, a pulse wave (gated sinusoid wave) initiated in homogenous air medium is simulated. A simple geometry model (Fig 6) is used that is similar to the 2D cylinder harmonic-analysis model except that the 2D cylinder is air. The purpose of using an air-filled cylinder submerged in air is to consider possible artifacts that might be caused by different meshes. The pulse is applied in air and propagates in the  $+x$  direction. The locations A ( $-0.9\lambda$ , 0), B ( $-0.65\lambda$ , 0), C ( $0.4\lambda$ , 0), H (0,  $0.4\lambda$ ) (in Fig 6) denote where the acoustic pressure waveforms are plotted in Fig 7 to evaluate mainly DPW and ITS.



### Parameters:

$f = 3 \text{ kHz}$   
 Air ( $c_{\text{air}} = 340 \text{ m/s}$ ,  $\lambda_{\text{air}} = 0.113 \text{ m}$ ,  $\rho_{\text{air}} = 1.2 \text{ kg/m}^3$ )  
 $\phi_{\text{inc}} = 0^\circ$   
 $P_{\text{inc}} = 1 \text{ Pa}$   
 DPW = variable  
 ITS = variable  
 $a = 0.4 \lambda_{\text{air}} = 45.2 \text{ mm}$   
 BOUND =  $a + 0.9 \lambda_{\text{air}}$  or  $a + 1.4 \lambda_{\text{air}}$

Fig 6: The wave propagation through air only. Locations A, B, C and H are denoted as red letters where A, B and C are on the x axis and H is on the y axis.

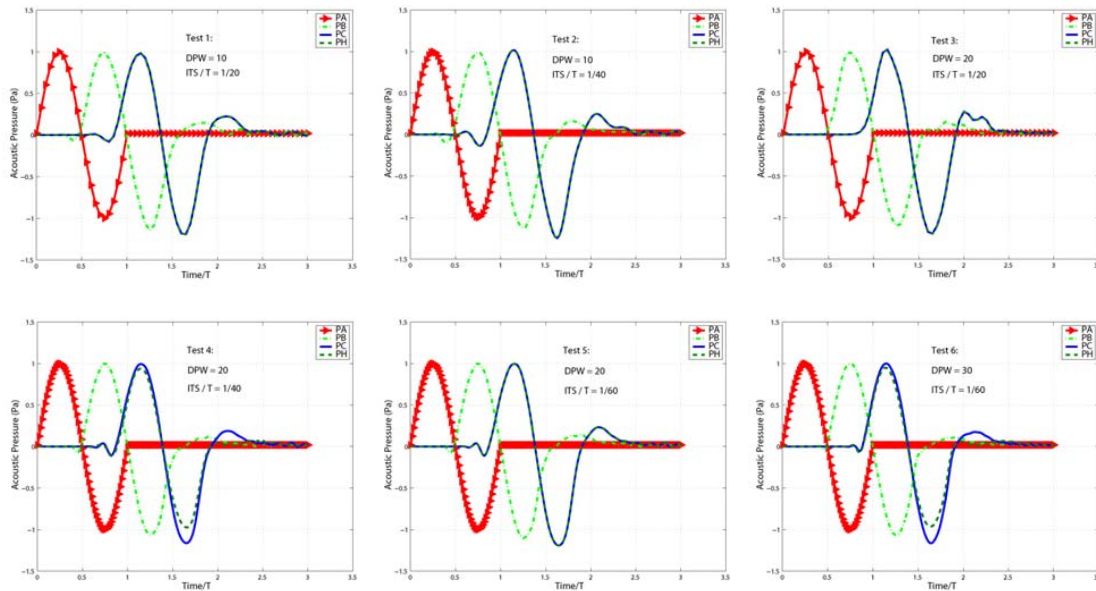


Fig 7: Pressure waveforms at four locations in homogeneous air medium to test DPW and ITS.

DPW (number of mesh divisions per wavelength, affects spatial resolution) and ITS (integration time step size, affects temporal resolution) are two key transient-analysis parameters, and BOUND (FEA absorbing boundary) determines the degree to which the computational domain can be assumed infinite in extent. Note: the incidence plane is located left of the center plane in the computation domain and BOUND affects the degree of the incident wave's distortion along the circular boundary of the computation domain. In general, the mesh must be fine enough to resolve the largest dominant frequency. A general guideline is to have at least 20 elements per wavelength along the propagation direction, that is,  $DPW \geq 20$  [ANSYS 6.1 Documentation: Modeling and Meshing Guide]. For transient analysis, using at least twenty points per cycle at the center frequency yields a reasonably accurate solution. ITS is given by  $ITS \leq T/DPW$ , where  $T = 1/f$ ,  $f$  is the center frequency of the incident pulse wave [ANSYS 6.1 Documentation: Transient Dynamic Analysis]. The acoustic absorbing boundary should be located at least  $0.2\lambda$  from the target object [ANSYS 6.1 Documentation: Coupled-Field Analysis Guide]. Six combinations of DPW, ITS, and BOUND were evaluated (Fig 7). It was observed that, in general, larger BOUND enhanced the computational accuracy (Tests 5 and 6 vs. Tests 1, 2, 3, and 4) while larger DPW and smaller ITS yield insignificant improvements (Test 2 vs. Test 1, Test 3 vs. Test 2). For future transient-analysis cases,  $DPW = 20$  and  $ITS = T/20$  will be considered to be sufficient and BOUND will be further evaluated in next section.

#### 4.5 2D Elastic Cylinder Shell (Transient Analysis Case)

Table 1 lists the properties for most components of human head [Goss 1978; Goss 1980; Duck 1990]. Among these properties, sound speed in air is the lowest and thus the wavelength in air is the shortest. Thus, for the FEA model, the smallest elements used are based on propagation in air. In the other words, to achieve good computation resolution for the mixed-property model, the optimal parameters for simulating propagation in air is determined.

Table 1: Material Properties in the Human Head

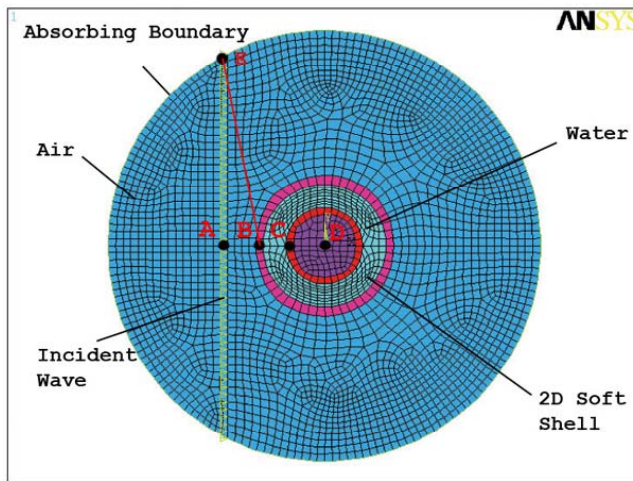
Material	Speed of Sound (m/s)	Densities (kg/m <sup>3</sup> )
Air	340	1.2
Water	1500	1000
Soft Tissues	1520-1580	980-1010
Lipid-based tissues	1400-1490	920-940
Collagen-based tissues	1600-1700	1020-1100
Aqueous humor	1002-1006	1500
Vitreous humor	1090	1530
Blood	1580	1040-1090
Brain – grey	1532-1550	1039
Brain – white		1043
Skull - compact inner and outer tables	2600-3100	1900
Skull - Spongy diploe	2200-2500	1000

A transient analysis on a 2D soft (elastic) cylinder shell is evaluated that includes property values of typical tissue (Table 1). Figure 8 shows the 2D soft shell geometry used in the simulations. In this case study, the effect of BOUND is further evaluated in object spaces of different sizes.

Two 2D cylinder shell tests were carried out with different FEA absorbing boundary on the same target object (Table 2).

Table 2: Small 2D Shell Transient Analysis

Parameters	Test 1	Test 2
Shell inner radius (a)	$0.1 \lambda_{\text{air}}$	$0.1 \lambda_{\text{air}}$
Shell thickness (d)	$0.025 \lambda_{\text{air}}$	$0.025 \lambda_{\text{air}}$
BOUND	$a + d + 0.5 \lambda_{\text{air}}$	$a + d + 2.5 \lambda_{\text{air}}$
Incident wave position	$-(a + d + 0.2) \lambda_{\text{air}}$	$-(a + d + 1.2) \lambda_{\text{air}}$
Distance between B and E (Fig 8)	$0.57 \lambda_{\text{air}}$	$2.56 \lambda_{\text{air}}$



Parameters:  
 $f = 3 \text{ kHz}$   
Outer medium: air ( $c_{\text{air}} = 340 \text{ m/s}$ ,  
 $\lambda_{\text{air}} = 0.113 \text{ m}$ ,  $\rho_{\text{air}} = 1.2 \text{ kg/m}^3$ )  
Inner medium: water ( $c_{\text{water}} = 1500 \text{ m/s}$ ,  
 $\rho_{\text{water}} = 1000 \text{ kg/m}^3$ )  
Soft Shell: ( $c_{\text{shell}} = 2800 \text{ m/s}$ ,  
 $\rho_{\text{shell}} = 1900 \text{ kg/m}^3$ )  
 $\phi_{\text{inc}} = 0^\circ$   
 $P_{\text{inc}} = 1 \text{ Pa}$   
DPW = 30  
ITS = T/30  
Computational length = 5 T  
BOUND = variable

Fig 8: The soft shell 2D FEA model generated in ANSYS.

Figure 9 shows x-axis acoustic pressure waveforms at locations A, B, C and D (Fig 8). The circular shape of the absorbing boundary causes distortion of the propagated wave along the boundary, and thus induces additional artificial incident waves along non +x-axis direction. When the absorbing boundary is positioned at a greater distance from the object, less undesirable interference reaches the target object in the same computational length scale. The distance between B and E (E is at the absorbing boundary; Fig 8) in Table 2 provides a rough estimate of the shortest possible time required for the interference wave to reach B from the absorbing boundary. Comparing the first period of the pressure waveform at B, the waveform in Test 2 is more symmetric than in Test 1. A reasonable explanation is that it requires about 0.5T for the interference wave at E to reach B in Test 1 whereas it requires about 2.5T in Test 2. It is also suspected that the significant variation of the pressure waveform shape at C in Test 1 at about 1T after the incident wave reaches C is due to the interference wave from the absorbing boundary reaching the target shell cylinder by that time. In Test 2, this interference is smaller, but still present, because it takes longer for the interfering waves at a further absorbing boundary location to reach the shell cylinder.

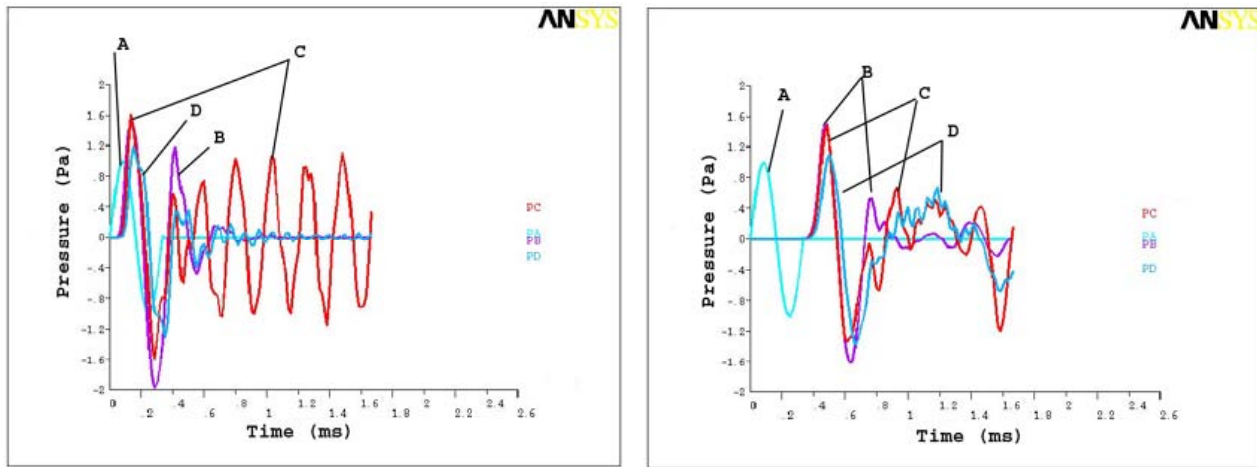


Fig 9: Acoustic pressure waveforms in Test 1 (a, left) and Test 2 (b, right)

To further demonstrate this observation, two large 2D shell cylinder tests were carried out with different FEA absorbing boundary (Table 3). In Test 3, the absorbing boundary is located the same distance from the shell cylinder as in Test 1. And in Test 4, the absorbing boundary is moved further away than in Test 3 but not as far as in Test 2.

Table 3: Large 2D Shell Transient Analysis

Parameters	Test 3	Test 4
Shell inner radius (a)	$0.58 \lambda_{\text{air}}$	$0.58 \lambda_{\text{air}}$
Shell thickness (d)	$0.09 \lambda_{\text{air}}$	$0.09 \lambda_{\text{air}}$
BOUND	$(a + d + 0.5) \lambda_{\text{air}}$	$(a + d + 1) \lambda_{\text{air}}$
Incident wave position	$-(a + d + 0.2) \lambda_{\text{air}}$	$-(a + d + 0.4) \lambda_{\text{air}}$
Distance between B and E (Fig 8)	$0.81 \lambda_{\text{air}}$	$1.34 \lambda_{\text{air}}$

Figure 10 shows x-axis acoustic pressure waveforms at locations A, B, C and D (Fig 8). In Test 4, an abnormal peak pressure amplitude occurs at C about 1T after the incident wave reaches this position, which is not observed in the other tests. Again it is very likely due to the interfering waves coming from the absorbing boundary. Similar to the previous small shell cylinder case, more symmetric pressure waveforms for the first period are found in Test 4. In both Tests 3 and 4, significant variation of the pressure waveform shape at B, C and D are observed about 1T after the incident wave reaches that position, which implies the absorbing boundary is not sufficiently further away from the shell cylinder. Based on the observations (§4.2 and §4.3), it is concluded that FEA absorbing boundary has a significant impact on the computation accuracy and larger BOUND is preferred to decrease the interference due to the circular absorbing boundary and to better simulate the incident plane wave.

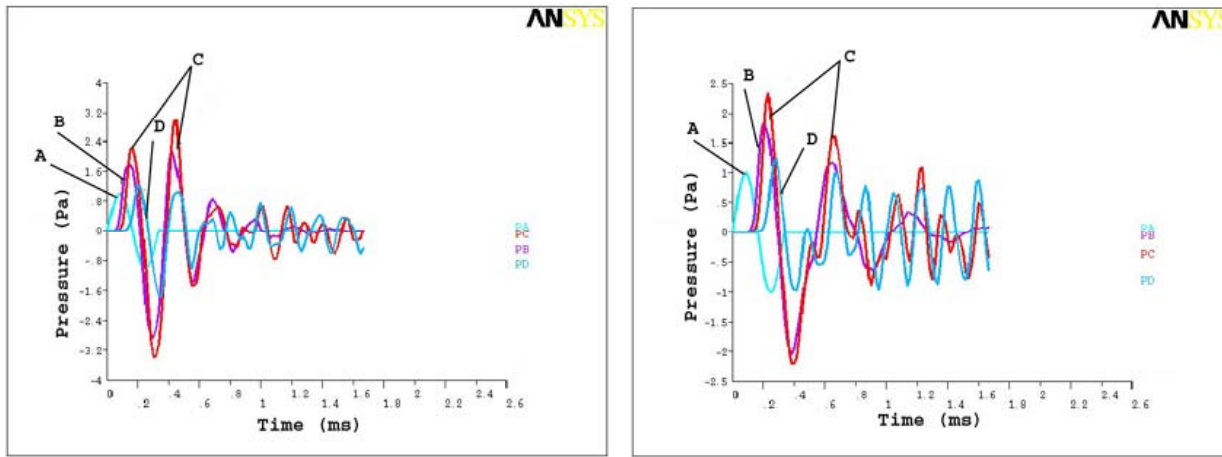


Fig 10: Acoustic pressure waveforms in Test 3 (a, left) and Test 4 (b, right)

### 4.6 3D Elastic (Water) Sphere (Transient Analysis Case)

In this case study, transient analysis is conducted on a 3D sphere of water that is submerged in air (§3.4), as shown in Fig 11. The acoustic pressure waveforms are shown at different locations (Fig 11) in Fig 12. The locations are A (0, 0, -0.9 $\lambda$ ), B (0, 0, -0.4 $\lambda$ ), C (0, 0, 0), D (0, 0, 0.4 $\lambda$ ). From the pressure waveforms it is determined that about 0.5 T is required for the incident wave to travel from A to B whereas the travel time is around 0.1 T from B to C. These travel time estimates agree with theory and thus validates the temporal accuracy of the FEA.

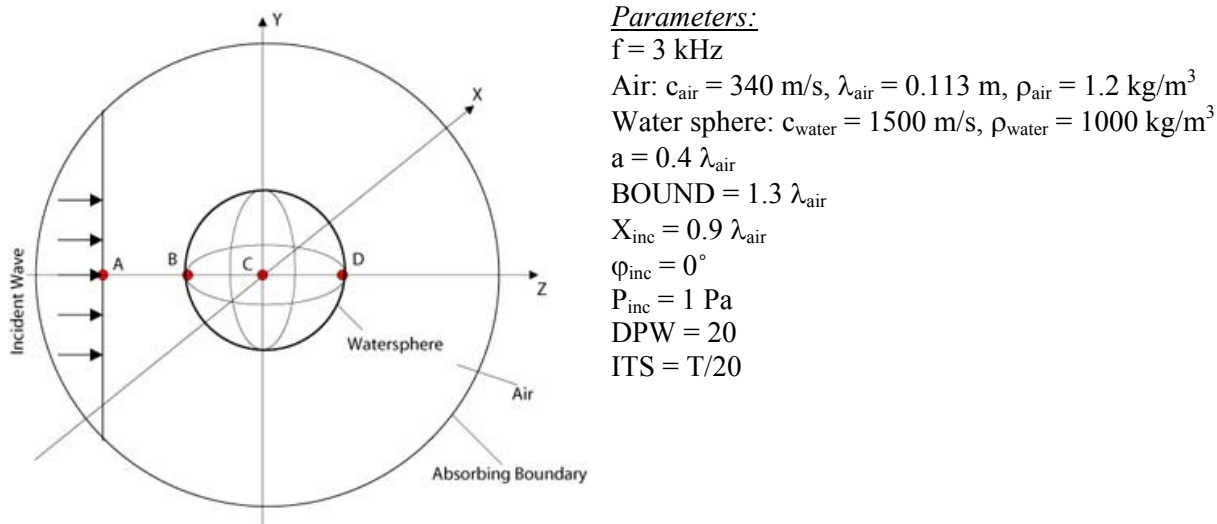


Fig 11: The 3D water sphere FEA model.

Furthermore, the instantaneous acoustic intensity was calculated based on the FEA acoustic pressure data from

$$I_A = \frac{p_A(t)^2}{\rho_{\text{air}} c_{\text{air}}}, \quad I_C = \frac{p_B(t)^2}{\rho_{\text{water}} c_{\text{water}}}, \quad (8)$$

where  $p(t)$  are the peak values of the acoustic pressure at their respective locations. The instantaneous acoustic intensity insertion loss (IL) from air to water was estimated from

$$IL_{\text{dB}} = 10 \log_{10} \left( \frac{I_{\text{peak},C}}{I_{\text{peak},A}} \right). \quad (9)$$

From the FEA data (Fig 12), the intensity loss from air to water was estimated to be -34 dB, a reasonable value relative to a theoretical loss estimate (-33 dB) for normal incidence at a planar air-water boundary.

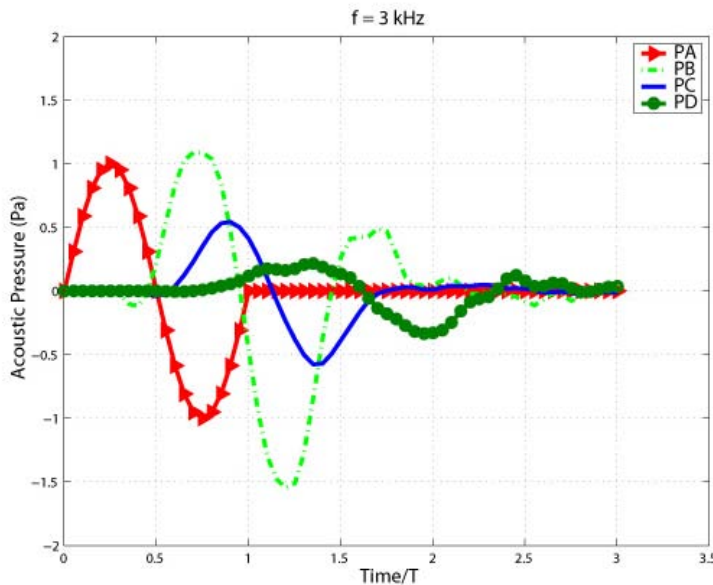


Fig 12: Acoustic pressure waveforms for the water sphere case at locations A, B, C, and D (Fig 11).

## 5.0 HUMAN-HEAD RELATED STUDIES

### 5.1 NIH Human Head

Transient FEA procedures of the 2D NIH human head (National Library of Medicine's Visible Human Project, National Institutes of Health, Bethesda, MD) have been constructed, simplified and verified. The male anatomic dataset was used. The anatomic dataset consists of 0.33-mm-wide transverse sections of the head, with each section 2048 pixels by 1216 pixels and each pixel 8-bit RGB scale. A simplified 2D human head analysis was conducted using one of the 0.33-mm-wide transverse sections. The first challenge (computational, not scientific) was to convert the NIH human head digital raster image dataset into a vector format file for import to ANSYS that uses IGES-format vector data. Then, the outer surface of the head was segmented to yield only the head contour. Skull was modeled as a 1-cm-thick layer immediately inside the human head contour. The interior region was modeled as water (Fig 13).

Transient (one-cycle sine wave) analyses were performed at 4 frequencies (0.125, 1, 3 and 10 kHz) and two incident angles (0°: towards the right side, and 45°: approximately towards the right cheek) (Fig 14).

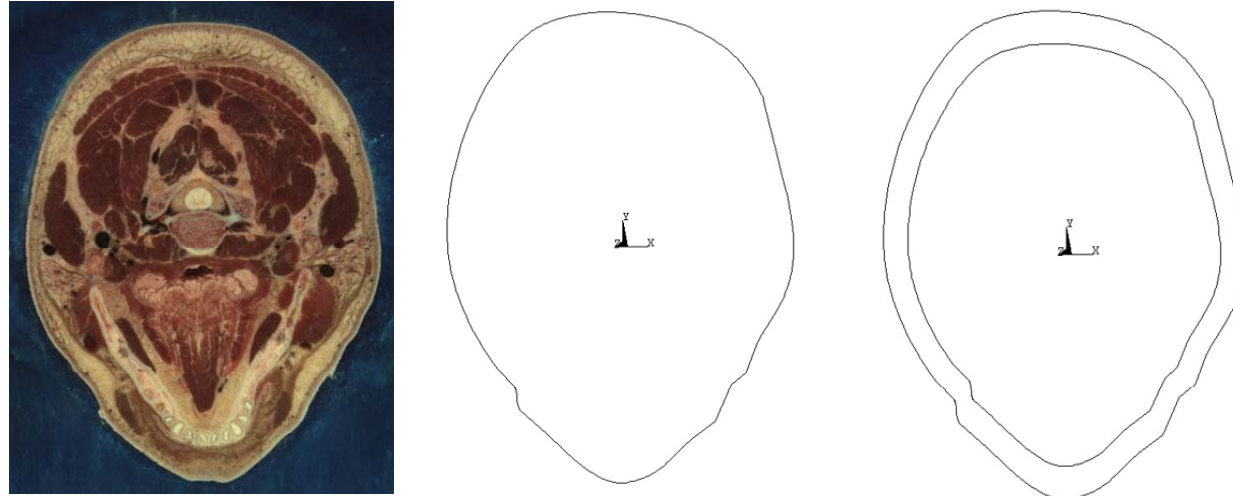
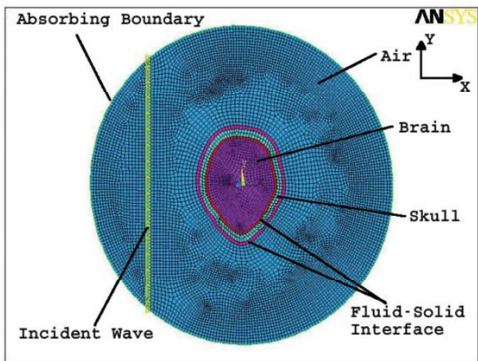


Fig 13: Development of two-dimensional geometric model of human head based on anatomic image.

The instantaneous acoustic pressure waveforms were recorded at 4 locations, A, C, F and H (Fig 15), which are at approximately the left and right ear locations near each side of the skull, and shown in Fig 16. Validation of the process was accomplished by estimating the acoustic intensity loss across the skull from the instantaneous acoustic pressure waveforms on each side of the skull (one location in air and the other location in water). The acoustic loss (Eqns 8 & 9; §4.5) across the skull was estimated from the FEA data to be approximately 26 dB, reasonably consistent with theoretical estimates (33 dB) considering this is a 2D analysis. The instantaneous acoustic intensities are shown in Fig 17 for two tests with same incident frequency (3 kHz) and the two incident angles (0° and 45°).

### 5.2 Analyze Human Head

The transient FEA procedure of the 3D Analyze (Mayo Clinic, Rochester, MN) human head model has also been demonstrated. The human head model was derived from the 3D Analyze MRI dataset. The Analyze human head outer surface was segmented slice-by-slice as shown in Fig 18.



*Parameters:*

Outer medium: air ( $c_{air} = 340$  m/s,  $\lambda_{air} = 0.113$  m,  $\rho_{air} = 1.2$  kg/m<sup>3</sup>)

Inner medium: water ( $c_{water} = 1500$  m/s,  $\rho_{water} = 1000$  kg/m<sup>3</sup>)

Human skull ( $\rho = 1412$  kg/m<sup>3</sup>, Young's modulus = 6.5 GPa, Poisson's ratio = 0.22) [Sauren 1993]

Human head: 15 mm x 20 mm

Skull thickness: 10 mm

BOUND = 7.5 mm + 2.0  $\lambda_{air}$

$X_{inc}$  = BOUND - 0.4  $\lambda_{air}$

$\varphi_{inc}$  = 0° or 45° (see Fig 14)

$P_{inc}$  = 1 Pa

DPW = 20

ITS = T/20

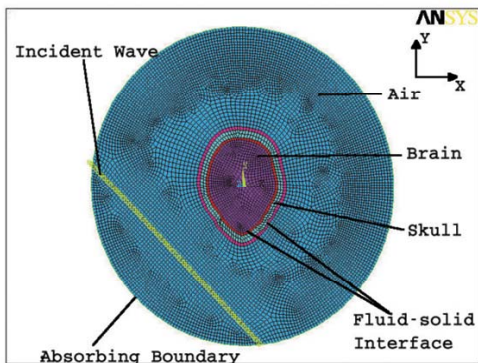


Fig 14: (a, top) Incident angle  $\varphi_{inc}$  = 0°. (b, bottom)  $\varphi_{inc}$  = 45°.

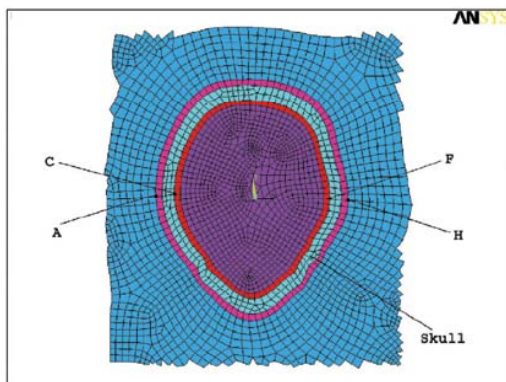


Fig 15: Four locations (A, C, F, H) along inner and outer skull surface which are at approximately the left and right ear locations near each side of the skull.

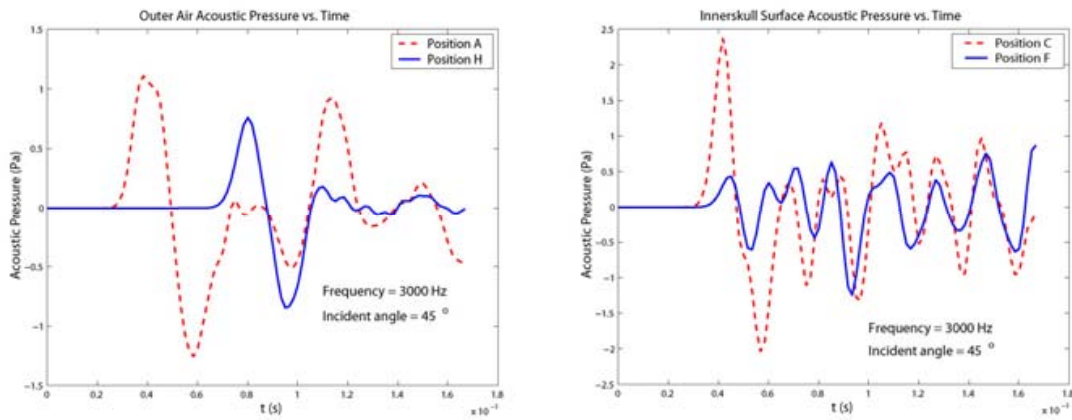


Fig 16: Instantaneous acoustic pressure waveforms recorded at four locations (see Fig 15).

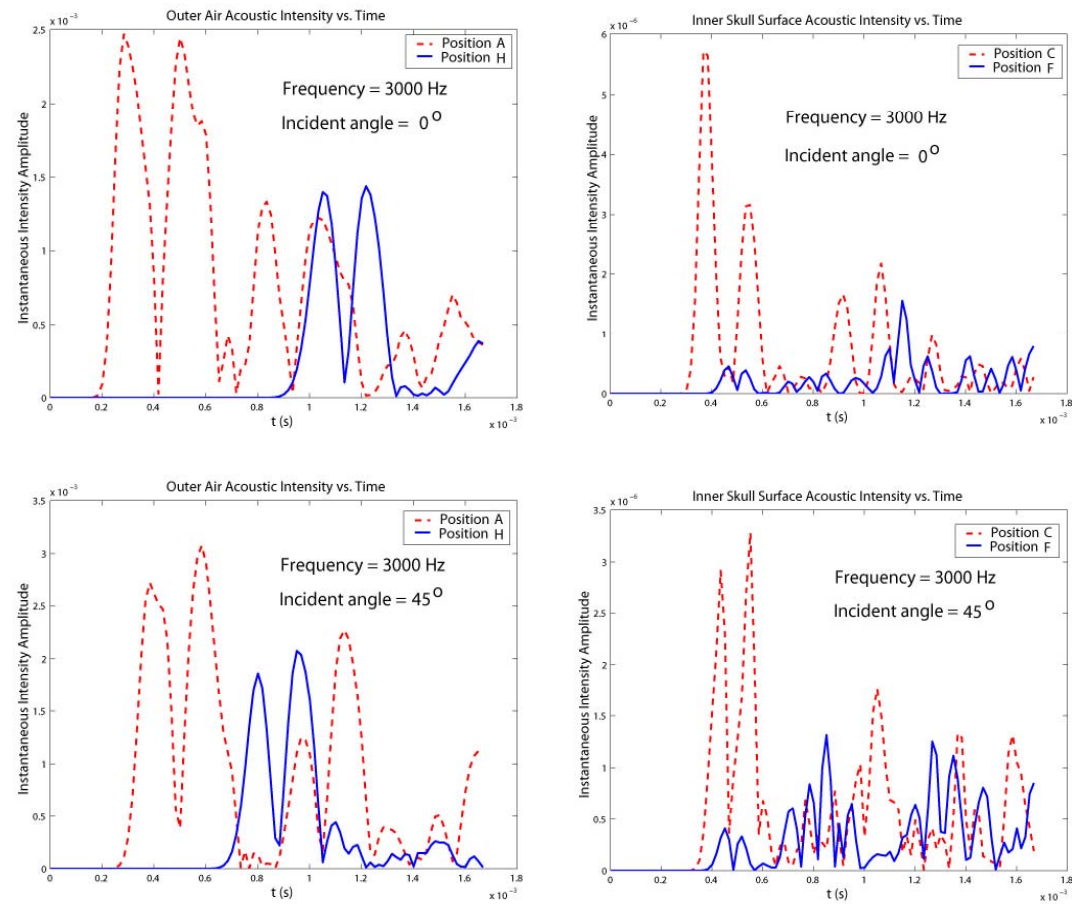


Fig 17: Instantaneous acoustic intensity distributions at a frequency of 3 kHz at four locations (see Fig 15). (top panels)  $\phi_{inc} = 0^\circ$  and (bottom panels)  $\phi_{inc} = 45^\circ$ .

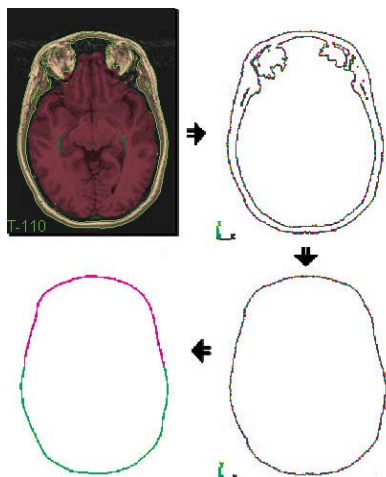
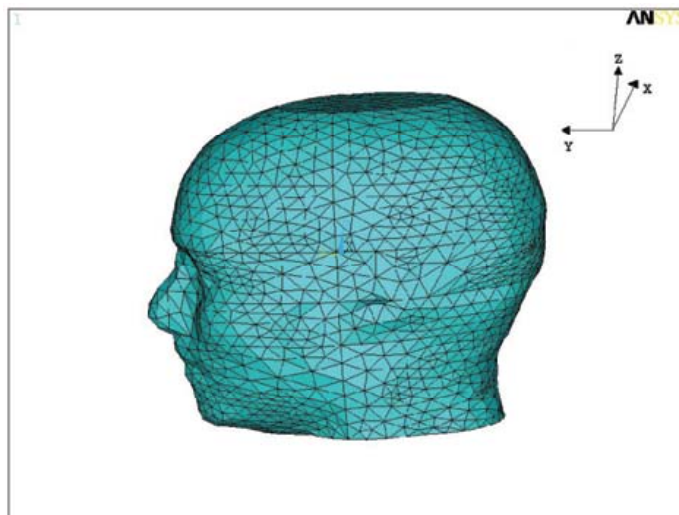


Fig 18: The Analyze human head MRI image slice is segmented to derive the outer head contour.

The Analyze human head model contains a large number of points (order:  $10^5$ ). Therefore, this model was further simplified (order: 10) while maintaining the original outer geometry. The material internal to the outer 3D head surface was constructed of skull material properties to demonstrate that it was feasible to quantify the sound pressure amplitude at a location within the head relative to the air-borne sound pressure amplitude. The 3D FEA model is shown in Fig 19.



#### Parameters:

Outer medium: air ( $c_{\text{air}} = 340 \text{ m/s}$ ,  
 $\lambda_{\text{air}} = 0.113 \text{ m}$ ,  $\rho_{\text{air}} = 1.2 \text{ kg/m}^3$ )

Inner medium: water ( $c_{\text{water}} = 1500 \text{ m/s}$ ,  
 $\rho_{\text{water}} = 1000 \text{ kg/m}^3$ )

Human skull ( $\rho = 1412 \text{ kg/m}^3$ ,  
Young's modulus = 6.5 GPa,  
Poisson's ratio = 0.22)

Human diameter:  $\sim 0.18 \text{ m}$

BOUND =  $0.09 \text{ m} + 0.9 \lambda_{\text{air}} = 0.192 \text{ m}$

$X_{\text{inc}} = \text{BOUND} - 0.4 \lambda_{\text{air}} = -0.1467 \text{ m}$

$P_{\text{inc}} = 1 \text{ Pa}$

ITS =  $T/20$

Fig 19: The 3D FEA human head model.

Admittedly this is an unrealistic realization of the head but one that can be evaluated in three dimensions and allows for the evaluation quantitatively of propagation into skull material. A transient 3-kHz one-cycle sine wave was incident from air onto the simple human head model and acoustic pressure waveforms were obtained at three locations (Fig 20). The instantaneous acoustic intensity peak (Eqn 8; §4.5) in air was determined to be about  $2.7 \text{ mW/m}^2$  and the acoustic intensity in the skull bone was about  $1.24 \mu\text{W/m}^2$ . The acoustic loss (Eqn 9; §4.5) across the 3D skull model surface was estimated to be approximately 32 dB, quite consistent with theoretical estimates (33 dB).

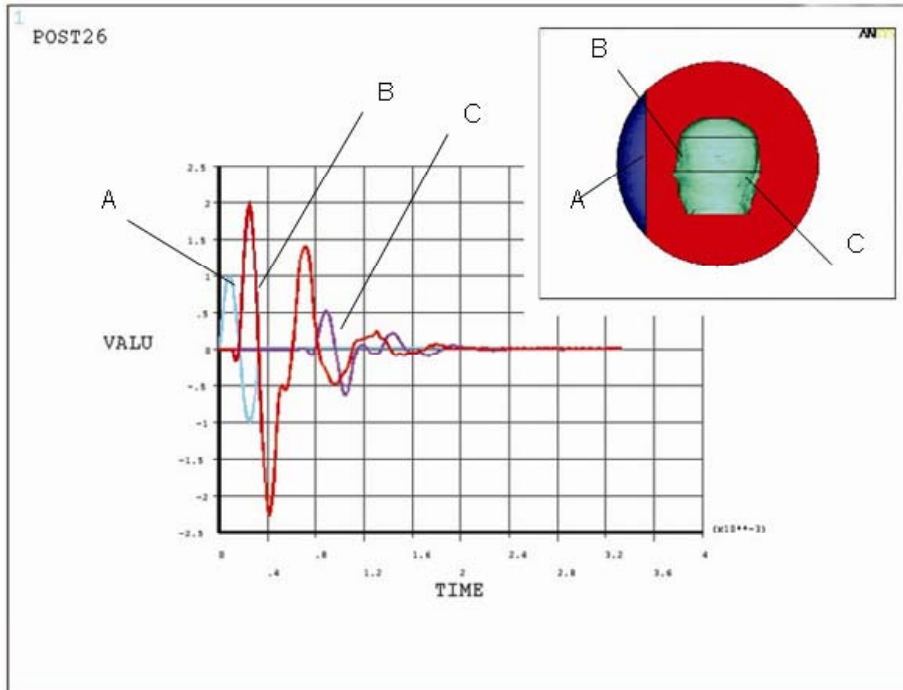


Fig 20: Acoustic pressure waveforms at three selected locations for the 3D FEA human head model.

These human head studies identified a problem that we knew we were going to have: how to represent graphically and quantitatively a 3D process? This work with the simpler Analyze human head model provided needed insight to represent a 3D process. Therefore, while the work continues to develop a 3D human head from the more complete NIH dataset, a procedure was initiated to represent graphically and quantitatively a 3D transient process.

### 5.3 Ray Tracing

A ray tracing approach to represent graphically and quantitatively a 3D transient process has been developed. Ray tracing is a common procedure by which wave propagation is displayed. For example, in the study of optics, rays are used to depict the path or paths taken as a light wave travels through a lens. However, in optics, the eikonal equation can be solved because the wavelength is assumed to be zero so that propagation laws can be formulated in terms of geometry. This is also the case for geometric acoustics and is often used to solve acoustic propagation problems in the ocean. However, for the case of an acoustic wave that has a wavelength comparable to the object onto which it is incident, the full wave equation must be solved because diffraction needs to be included as part of the analysis. Therefore, ray paths need to be deduced from the propagated acoustic wavefront. The transient ANSYS FEA procedure yields data from which the propagated acoustic wavefront has been deduced. From the propagated acoustic wavefront, rays have been calculated by taking the normal components of the wavefront surface as a function of time. The transient FEA procedure yields data as a function of time steps, thus allowing the wavefront to be animated as a function of time. Also, from these data, as long as the time steps are sufficiently small, ray paths can be calculated. Further, after the ray paths have been calculated, the acoustic energy can be determined from the density (number of ray paths that intersect a unit volume) of ray paths in a particular volume.

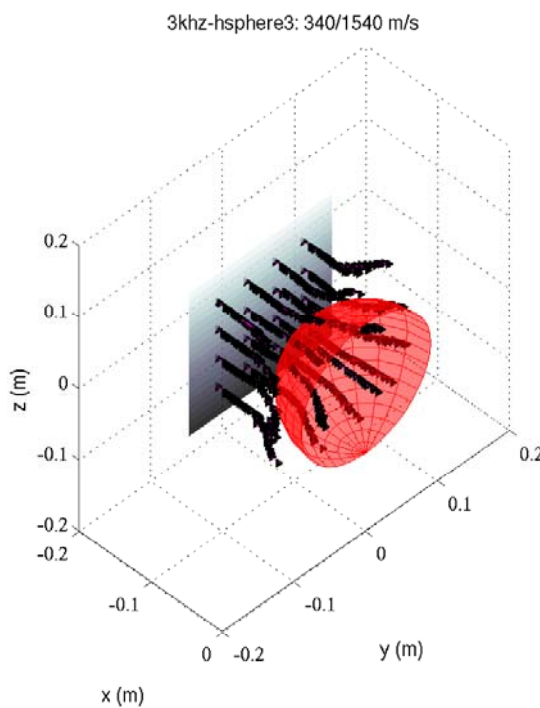
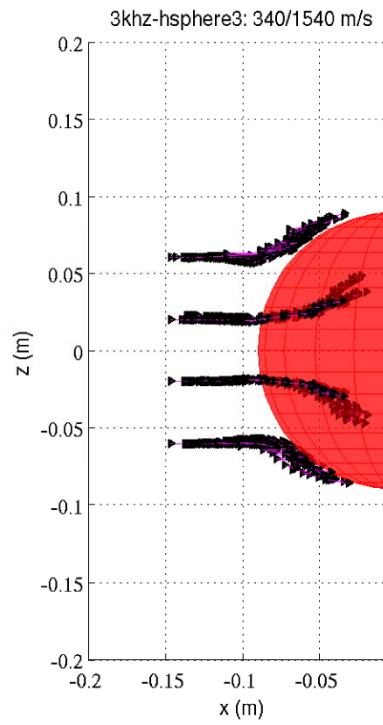
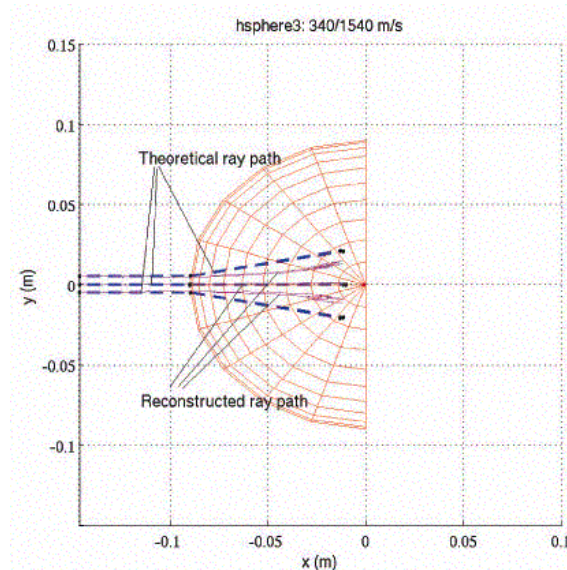


Fig 21: Ray paths calculated based on FEA data.

Transient (3-kHz one-cycle sine wave) ANSYS FEA procedures were performed using a 9-cm-radius hemisphere of known propagation speeds. The plane wave was incident in air (speed = 340 m/s) onto the spherical surface of the hemisphere that had propagation speeds consistent with water (speed = 1540 m/s). Wavefronts were deduced from a time-domain correlation technique. From the wavefronts, ray paths were calculated (Fig 21 depicts ray paths). The ray paths originated in air and propagated into the hemisphere. For low-angle incidence, the ray path directions into the hemisphere were consistent with those calculated from Snell's Law. However, as the angle of incidence onto the hemisphere increased, the ray path directions into the hemisphere became progressively greater from those expected from a Snell's Law calculation. We are currently investigating the cause of this phenomenon. We suspect that the ray path directions are correct because diffraction phenomenon could be causing this problem. For this example, the wavelength in air is 11.3 cm (radius of the hemisphere is 9 cm) and  $ka$  is 5.0 (all based on a center frequency of 3 kHz but the frequency content of the one-cycle wave is much broader). To test our hypothesis, we conducted the transient ANSYS FEA analysis at 10 kHz using the 9-cm-radius hemisphere. However, at the high frequency of 10 kHz, we hit the current ANSYS version limits on elements/nodes number and a coarse meshing is used in the FEA model that compromised the computation accuracy. Comparing the computational results and the theoretical solutions calculated using Snell's law, up to 0.7° difference is found for low-angle incidence while up to 10° difference is found for larger-angle incidence (Fig 22). The next step is to conduct the FEA analysis using planar surfaces as a function of incident angle. A well-documented and verified ray tracing procedure will provide an easy to understand (and visualize) dynamic process. Also, the budget requests funds to support partially the unlimited ANSYS version.



**Fig 22: Ray path for the hemisphere model.**

Figure 23 shows the wavefront at three time steps as the wavefront propagates through the hemisphere. If the shown arrows were connected at each wavefront step, the resultant lines would depict ray paths.

In summary, we have (1) validated finite-element analysis (FEA) general processing code for both harmonic and transient solutions, (2) constructed, simplified and verified transient FEA analyses of the 2D NIH human head, (3) demonstrated FEA analysis of the 3D Analyze human head, and (4) developed a ray tracing approach to graphically and quantitatively represent a 3D transient process.

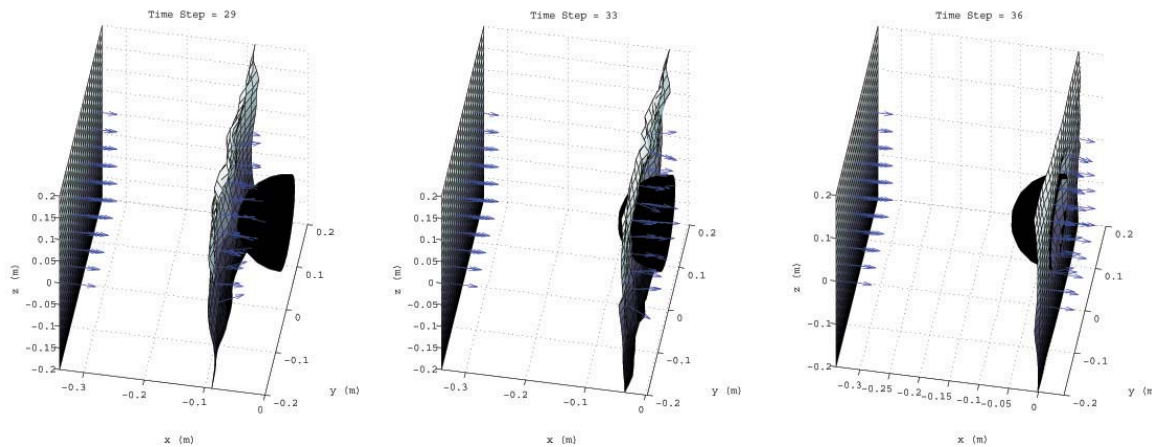


**Fig 23. Three time steps as the wavefront propagates through the hemisphere.**

## 6.0 ACKNOWLEDGMENT

Support for this work from the US Air Force Office of Scientific Research through US/AFOSR Award # F 49620-03-1-0188 is acknowledged.

## 7.0 REFERENCES

[Békésy, 1948] G von Békésy, "Vibration of the head in a sound field and its role in hearing by bone conduction," *Journal of the Acoustical Society of America*, 20, 1948, 749-760.

[Barany 1938] E. A. Barany, "A contribution to the physiology of bone conduction," *Acta Otolaryngol Suppl*, 26, 1938, 1-223.

[Duck 1990] F. A. Duck, *Physical properties of tissues: A comprehensive reference book*, New York, NY: Academic Press, 1990.

[Freeman 2000] S. Freeman, J.-Y. Sichel, H. Sohmer, "Bone conduction experiments in animals -- evidence for a non-osseous mechanism," *Hearing Research*, 146, 2000, 72-80.

[Goss 1978] S. A. Goss, R. L. Johnston, F Dunn, "Comprehensive compilation of empirical ultrasonic properties of mammalian tissues," *Journal of the Acoustical Society of America*, 64, 1978, 423-457.

[Goss 1980] S. A. Goss, R. L. Johnston, F Dunn, "Compilation of empirical ultrasonic properties of mammalian tissues - II," *Journal of the Acoustical Society of America*, 68, 1980, 93-108.

[Guild 1936] S.R. Guild, "Hearing by bone conduction: the pathways of transmission of sound," *Ann Otol Rhinol Laryngol*, 45, 1936, 736-754.

[Morse 1968] P. M. Morse and K. U. Ingard, *Theoretical acoustics*, New York, NY: McGraw Hill, 1968.

[OSHA 1910.95]. Occupational noise exposure. Standard number 1910.95, Occupational Safety & Health Administration, U.S. Department of Labor, Washington, DC

## Evaluation of Acoustic Propagation Paths into the Human Head

---

[Pierce 1989] A. D. Pierce, Acoustics: An introduction to its physical principles and applications, Woodbury, NY: Acoustical Society of America, 1989.

[Sauren 1993], A. H. J. Sauren and M. H. A. Classens, “Finite element modeling of head impact: The second decade”, International IRCOBI Conference on Biomechanics of Impacts Eindhoven, 241-254, September 8-10, 1993, Eindhoven, the Netherlands.

[Sohmer 2000] H. Sohmer, S. Freeman, M. Geal-Dor, C. Adelman, I. Savion, “Bone conduction experiments in humans – a fluid pathway from bone to ear,” Hearing Research, 146, 2000, 81-88.

[Sohmer 2004] H. Sohmer, S. Freeman, “Further evidence for a fluid pathway during bone conduction auditory stimulation,” Hearing Research, 193, 2004, 105-110.

[Stefan 2004] S. Stefan, N. Hato, R. L. Goode, “Fluid volume displacement at the oval and round windows with air and bone conduction stimulation,” Journal of the Acoustical Society of America, 115, 2004, 797-812.

[Wever 1954] E. G. Wever and M. Lawrence, Physiological acoustics, Princeton, NJ: Princeton University Press, 1954.

[Zwislocki 1957] J. Zwislocki, “In search of the bone-conduction threshold in a free sound field,” Journal of the Acoustical Society of America, 29, 1957, 795-804.